

# Photonic “hourglass” design beyond the standard bulk model of phonon decoherence

José Ferreira Neto,\* Benedek Gaál, Luca Vannucci, and Niels Gregersen

*Department of Electrical and Photonics Engineering, Technical University of Denmark, 2800 Kgs. Lyngby, Denmark*

(Dated: July 25, 2024)

We study the impact of mechanical vibrations on the performance of the photonic “hourglass” structure, which is predicted to emit single photons on-demand with near-unity efficiency and indistinguishability. Previous investigations neglected the impact of vibrational modes inherent to this quasi-1D geometry, relying instead on a three-dimensional bulk assumption for the phonon modes. However, it has been shown that phonon decoherence has a much stronger impact in 1D structures as compared with bulk media. Here, we surprisingly demonstrate the robustness of the photonic hourglass design, achieving close-to-unity indistinguishability even by incorporating a detailed description of the vibrational modes. We explain this unexpected result in terms of the large Purcell enhancement of the hourglass single-photon source, which eliminates the negative effect of phonons. Our findings highlight the key role of high- $Q$  optical cavities in mitigating the detrimental effect of phonon decoherence, even for structures of reduced dimensionality.

## I. INTRODUCTION

Within quantum physics, the pursuit of quantum computing has been a long-sought goal [1, 2]. Among the various physical platforms proposed, the photonic quantum computer stands out as a particularly promising avenue [3–6]. Here, a key component is the single-photon source (SPS) allowing for directional, triggered emission and efficient collection of highly pure indistinguishable single photons acting as carriers of quantum information. The figures of merit include [7, 8] the photon indistinguishability  $\mathcal{I}$ , which measures the degree to which photons emitted from the source are quantum-mechanically identical, reflecting their capacity to coalesce into a two-photon state in a Hong-Ou-Mandel experiment [9], and the photon collection efficiency  $\varepsilon$ , defined as the probability that the collecting optics captures a photon emitted by the source. While highly indistinguishable photon emission can be achieved using spontaneous parametric down-conversion [10], this process is probabilistic, limiting the efficiency to a few percent.

As an alternative, the semiconductor quantum dot (QD) positioned inside a tailored photonic environment has recently emerged as a successful strategy [8, 11] for deterministic single photon generation. Indeed, by placing the QD inside an optical cavity and exploiting cavity quantum electrodynamics (cQED), highly efficient emission  $\varepsilon \sim 0.6$  [12–14] of single indistinguishable photons has been demonstrated. However, the cQED approach suffers from an inherent trade-off [15] between the achievable efficiency and indistinguishability in the presence of phonon-induced decoherence, limiting the achievable product  $\mathcal{I}\varepsilon$  for the micropillar SPS to  $\sim 0.95$  [16].

It was recently shown that the hybrid photonic nanowire-micropillar hourglass design [17, 18] sketched

in Fig. 1 allows circumventing this trade-off by exploiting suppression of the background emission [19], and a product  $\mathcal{I}\varepsilon \sim 0.973$  [18] was predicted with a computed indistinguishability  $\mathcal{I}$  above 0.99. This prediction of the indistinguishability in the presence of phonon-induced decoherence was obtained using a Born-Markov polaron master equation for bulk media [15, 18]. This approach models the dynamics of an open quantum system interacting with a memoryless phonon reservoir, where the interaction with the mechanical environment of the hourglass structure is assumed to be the same as for a 3D bulk structure. However, it was recently shown [20] that low-dimensional structures, in particular the 1D wire geometry, feature significantly reduced indistinguishability compared with a 3D bulk medium, thus questioning the validity of the mechanical model and the corresponding high indistinguishability reported in Ref. [18].

In this work, we investigate the two-photon indistinguishability  $\mathcal{I}$  of the photonic hourglass structure in the presence of temperature-induced dephasing via

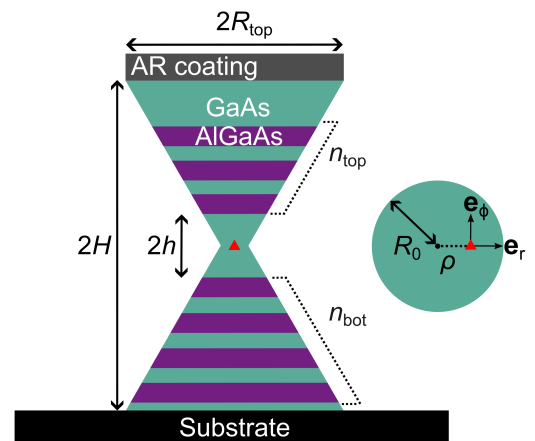


FIG. 1: The hourglass structure hosting a pyramidal QD (red triangle) and beam waist cross-section featuring an off-axis dipole displaced from the center by  $\rho$ .

\* jofer@dtu.dk

longitudinal acoustic phonons using a model of the phonon spectral density accounting for the discrete set of mechanical vibration modes of the hourglass structure. In particular, we elucidate whether or not the trade-off [15] between  $\varepsilon$  and  $\mathcal{I}$  can still be circumvented by the proper structuring of the photonic environment [18] when fully taking into account the lattice vibrations characteristic of a low-dimensional geometry.

## II. GEOMETRY

The geometry of our photonic hourglass structure is illustrated in Fig. 1 with geometric parameters almost identical, except for a larger number of DBR layer pairs in our bottom DBR, to those in Ref. [18]. The cavity, formed from 11 (48) distributed Bragg reflector (DBR) pairs in the top (bottom) mirror, is designed to operate at a wavelength  $\lambda = 925$  nm, a typical emission wavelength for InAs/GaAs QDs. At the position of the QD, the design features a narrow diameter of  $2R_0 = 228$  nm combined with a large top diameter  $2R_{\text{top}} = 1860$  nm. The total height of the structure  $h_{\text{total}} = 2H + t_{\text{AR}} \sim 117$   $\mu\text{m}$ , where  $H = 58.5$   $\mu\text{m}$  and the thickness of the anti-reflection (AR) coating  $t_{\text{AR}} = \lambda/4n_{\text{eff,AR}}$  [18]. The exceptionally high aspect ratio of  $\sim 513$  is due to the very small sidewall angle required to ensure adiabatic mode expansion [17, 21]. This aspect ratio greatly exceeds the one of a typical micropillar SPS [16, 22, 23], suggesting that a 3D description of the vibrational modes may indeed be inaccurate. The refractive indices of the alternating DBR layers are  $n_{\text{AlGaAs}} = 2.9895$  and  $n_{\text{GaAs}} = 3.4788$ , while  $n_{\text{AR}} = \sqrt{n_{\text{GaAs}}}$ . Additional material parameters are given in Table A in the SI (Supplementary Information).

## III. MODEL

Our primary goal is to evaluate the performance of the hourglass structure predicted to feature very high indistinguishability ( $\mathcal{I} > 0.99$ ) under a 3D bulk phonon assumption. Thus, to distinguish between optical and mechanical contributions to the performance, we consider two distinct structures: (i) the optimized structure with DBRs, as depicted in Fig. 1, and (ii) the geometry without DBRs, where the entire hourglass geometry is instead homogeneously composed of GaAs material.

Assuming a perfectly antibunched photon output and an initially excited emitter, we can calculate the two-photon indistinguishability  $\mathcal{I}$  as [24]

$$\mathcal{I} = \Gamma \int_0^\infty dt e^{-\Gamma t} |P(t)|^2, \quad (1)$$

where we consider the emission rate into the cavity  $\Gamma = \Gamma_{\text{C}} = F_{\text{p}}\Gamma_{\text{Bulk}}$ , which is enhanced by the Purcell factor  $F_{\text{p}}$  relative to its value  $\Gamma_{\text{Bulk}}$  in a bulk

medium, and where we assume  $\Gamma_{\text{Bulk}} = 1$  GHz. As discussed in detail in Appendix A, the QD coherence evolution is given in an independent boson model by  $P(t) = e^{\Phi(t)}$ , where the phonon propagator  $\Phi(t) = \sum_m -\theta_m^2 \sin^2(\omega_m t/2) - \eta_m^2 (1 - e^{-i\omega_m t})$ . Here,  $\omega_m$  are the mechanical eigenfrequencies with associated QD coupling parameters  $\theta_m$  and  $\eta_m$  defined in Appendix A.

The modulation of the QD bandgap via deformation potential is given by [25, 26]

$$\hbar \frac{\partial \omega_{\text{eg}}}{\partial u_m} = a \left( \frac{\partial \epsilon_{\text{h}}}{\partial u_m} \right) + \frac{b}{2} \left( \frac{\partial \epsilon_{\text{sh}}}{\partial u_m} \right), \quad (2)$$

where our pyramidal QD experiences a residual bi-axial compressive strain given by the hydrostatic  $\epsilon_{\text{h}} = \epsilon_{xx} + \epsilon_{yy} + \epsilon_{zz}$  and the tetragonal shear  $\epsilon_{\text{sh}} = 2\epsilon_{zz} - \epsilon_{xx} - \epsilon_{yy}$  ( $z$  is the QD growth axis) strain contributions, with  $a$  and  $b$  corresponding to the associated deformation potentials of the QD material, respectively. Here, we suppose that the QD is composed of an  $\text{In}_{0.5}\text{Ga}_{0.5}\text{As}$  alloy and use  $a = -7.5$  eV and  $b = -1.9$  eV (linear interpolation between the deformation potentials on InAs and GaAs [27]).

The vibrational properties, including the mechanical eigenfrequencies  $\omega_m$  for the free-standing geometry (singly-clamped to a substrate), their effective mass  $m_m^{\text{eff}}$  (see SI for more details), and primary strain tensors ( $\epsilon_{xx}$ ,  $\epsilon_{yy}$ ,  $\epsilon_{zz}$ ), were calculated with the finite element method (FEM) software COMSOL Multiphysics. The strain tensors are extracted at points along the beam waist cross-section defined by the direction of maximum displacement, i.e., at a height  $H$  from the substrate, as shown in Fig. 1. The retrieved modes are then classified as flexural ( $F$ ), longitudinal ( $L$ ), or torsional ( $T$ ) so that we can properly account for their contributions.

We perform an assessment of the coupling parameters  $\eta_m^2 = (g_m/\omega_m)^2$  and  $\theta_m^2 = 4\eta_m^2 N_m$ , where  $N_m$  represents the phonon occupation number. These parameters indicate phonon emission in the zero-temperature limit and thermally-induced absorption, respectively. Among the first 101 modes analyzed (ranging up to 140 MHz), 80 exhibit flexural behavior (consisting of orthogonal flexural doublets [28]) while 21 are longitudinal. The upper panel of Fig. 2 illustrates 40 flexural modes vibrating along the same axis, whereas the lower panel features modes with longitudinal behavior. By comparing the mechanical frequencies and their associated couplings for both structures, i.e., with and without DBRs, it becomes clear that they display very similar results from a purely *mechanical* point of view. The exact values for the resonance frequencies of both flexural and longitudinal modes, along with their corresponding coupling strengths, are presented in Tables B and C in the SI.

We evaluate the Purcell factor  $F_{\text{p}}$  and the efficiency  $\varepsilon$  using an open-geometry Fourier Modal Method (FMM) [29, 30], where the QD at the position  $\mathbf{r}_0$  is modeled as a point dipole  $\mathbf{p}\delta(\mathbf{r} - \mathbf{r}_0)$  with in-plane polarization  $\mathbf{p}$ . The efficiency is computed using a single-mode model given by  $\varepsilon = \beta\eta$  [18, 21]. Here, the spontaneous emission

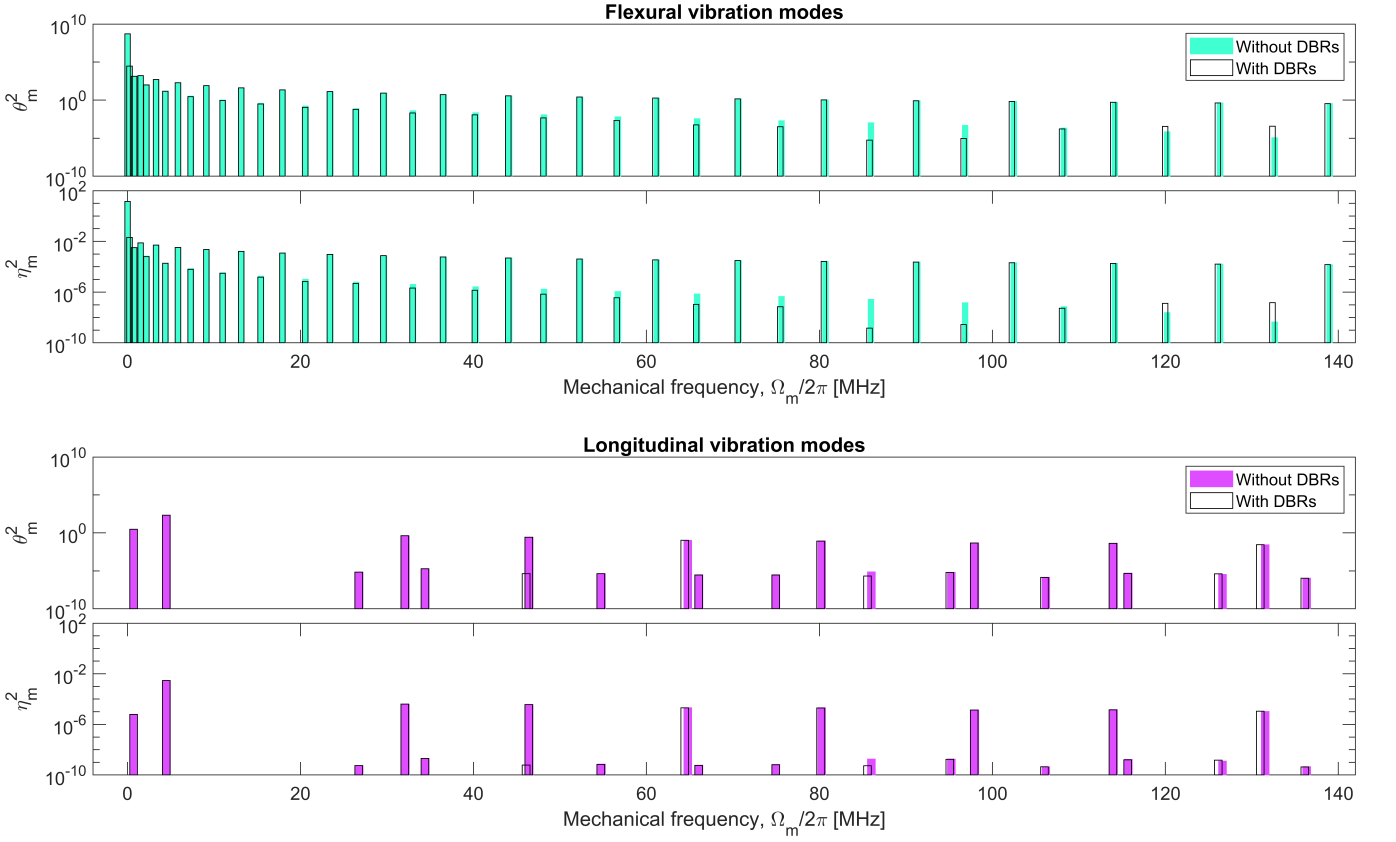


FIG. 2: Examining the impact of thermally-induced vibrations on the photonic hourglass structure at a temperature of  $T = 4$  K, we present the parameters  $\theta_m^2$  and  $\eta_m^2$  for all considered vibration modes. For flexural modes, we illustrate the maximum, on-sidewall values. In contrast, we depict the on-axis results for longitudinal modes, as they contribute more significantly to the  $\epsilon_{zz}$  strain component.

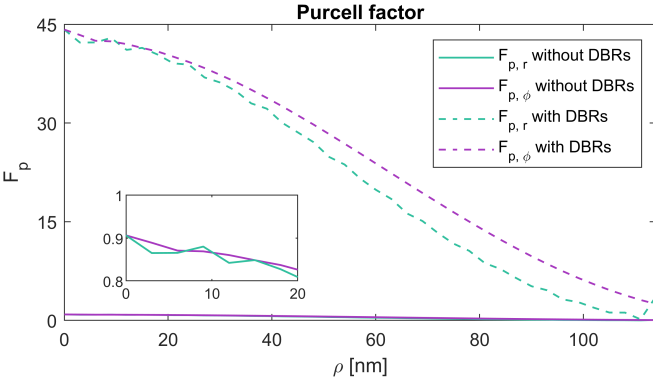


FIG. 3: Computed Purcell factor  $F_p$  for a dipole with a given polarization as a function of its radial displacement from the center. Here, the subscript  $r$  ( $\phi$ ) corresponds to a radial (azimuthal) linear optical dipole. Inset: magnified view of  $F_p$  for the structure without DBRs.

$\beta$  factor describes the fraction of light emitted into the cavity given by  $\beta = \frac{\Gamma_C}{\Gamma_T} = \frac{\Gamma_C}{\Gamma_C + \Gamma_B}$ , where  $\Gamma_T = \Gamma_C + \Gamma_B$  is the total emission rate including the contribution  $\Gamma_B$  to background modes. Additionally, the transmission  $\eta$

describes the power detected by a collection lens with specific numerical aperture (NA), taking into account an overlap with a Gaussian profile [31, 32], relative to the power in the cavity. This single-mode model provides an excellent description [18] of the efficiency combined with physical insight into the governing physics.

The predicted Purcell factor for both radial and azimuthal dipoles as a function of the offset displacement  $\rho$  is presented in Fig. 3. The structure with no DBRs exhibits no field enhancement at all ( $F_p < 1$ ), while the hourglass including DBRs features a maximum value of  $F_p \sim 45$  for  $\rho = 0$ . For both structures and dipole orientations, the enhancement drops with  $\rho$ , essentially following the electric field profile of the lateral profile of the fundamental  $HE_{11}$  mode. However, thanks to suppression [18, 19] of the background emission occurring for the small diameter  $2R_0 = 228$  nm at the position of the QD, we have  $\Gamma_B \sim 0.05\Gamma_{\text{Bulk}}$  for a QD in the center, and the hourglass thus does not rely on strong Purcell enhancement to maintain a high efficiency. Indeed, the computed efficiency presented in Fig. 4 remains large ( $\epsilon > 0.85$ ) for the hourglass with DBRs even for large displacements  $\rho$ , where the Purcell factor is modest, indicating good tolerance towards spatial misalignment.

Similar tolerance is observed in the absence of DBRs, albeit for corresponding lower efficiency. The different behaviors for the two dipole orientations in Fig. 4 for large  $\rho$  result from the different boundary conditions experienced by the two electric field components at the semiconductor-air interface.

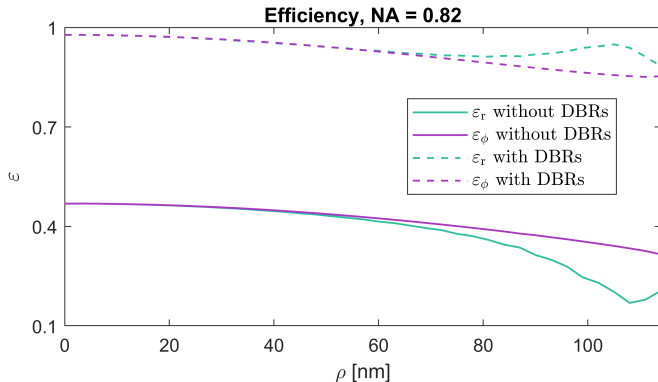


FIG. 4: Computed collection efficiency  $\varepsilon$  for a radial (azimuthal) linear optical dipole as a function of its radial offset position  $\rho$ . The solid curves give the extraction efficiency accounting for a Gaussian overlap.

#### IV. RESULTS

We now present the photon indistinguishability predicted from our model taking into account the discrete set of mechanical modes as a function of temperature in Fig. 5. In the absence of DBRs, the indistinguishability is indeed strongly decreased due to interaction with flexural and longitudinal vibration modes. For a QD approaching the sidewall, it drops below 0.1 at 4 K in agreement with previous results [20, 24]. However for the full hourglass structure including DBRs, we observe that  $\mathcal{I} > 0.99$  over the entire temperature range for a QD in the center, indicating excellent resilience of the hourglass structure towards phonon decoherence in spite of the low-dimensional nature of the geometry. We attribute this surprisingly good performance to the significant Purcell enhancement offered by the cavity. Indeed, the indistinguishability is reduced for a QD on the sidewall due to the low  $F_p$  for increasing  $\rho$  as discussed above.

We summarize our predicted SPS figures of merit for the four configurations, on axis/sidewall and with/without DBRs, at 4 K in Table I. The lack of DBRs and Purcell enhancement results in reduced efficiency with some tolerance towards spatial misalignment. The flexural mechanical modes of the structure, representing the primary source of decoherence, do not couple with a QD in the center, resulting in indistinguishability of 0.821 at 4 K comparable to that in a bulk medium [15]. For a displaced QD at the sidewall, the interaction with these flexural modes almost completely ruins the indistinguishability for the structure without DBRs. In

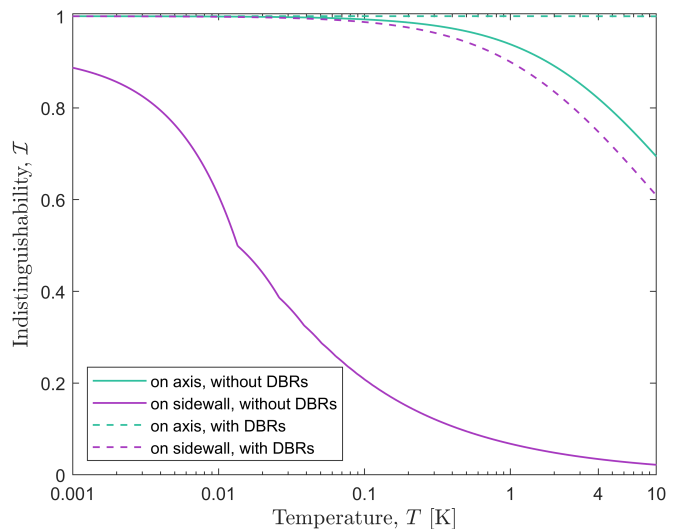


FIG. 5: Photon indistinguishability  $\mathcal{I}$  with respect to the operation temperature for a QD located either perfectly on the neutral axis or on the sidewall of the structure for the two contemplated designs (with and without DBRs).

contrast, for the full hourglass structure with DBRs, this picture completely changes, and near-unity performance is obtained on-axis with  $\varepsilon = 0.978$  and  $\mathcal{I} = 0.9999$ . While the tolerance of the indistinguishability towards spatial misalignment is not as good as for the efficiency, we still observe that a product  $\mathcal{I}\varepsilon = 0.66$  is obtained for a QD on the sidewall. Clearly, in practice, other effects, such as the detrimental influence of defect states near the semiconductor-air surface, will reduce this performance. Nevertheless, we observe that in the presence of cQED effects, the high aspect ratio and the 1D mechanical nature of the hourglass structure do not necessarily lead to strong phonon-induced decoherence, and the conclusion that background emission engineering [18] can circumvent the trade-off [15] between efficiency and indistinguishability remains valid even for a mechanical structure of low dimensionality.

Figure of merit	Without DBRs		With DBRs	
	On axis	On sidewall	On axis	On sidewall
$F_p$	0.91	0.08	44.20	3.66
$\varepsilon$	0.469	0.207	0.978	0.883
$\mathcal{I}$	0.821	0.034	0.9999	0.748
$\mathcal{I}\varepsilon$	0.385	0.010	<b>0.978</b>	0.660
Configuration	(a)	(b)	(c)	(d)

TABLE I: Overview of SPS figures of merit for a radial dipole at  $T = 4$  K with  $\text{NA} = 0.82$ .

## V. CONCLUSION

To conclude, we have implemented a model for phonon-induced coherence fully taking into account the discrete set of mechanical modes of a low-dimensional photonic structure, and we have used it to evaluate the achievable indistinguishability of the hourglass SPS. While the indistinguishability of the bare structure without DBRs is indeed strongly affected by, in particular, the set of flexural vibration modes in consistency with the literature, our model predicts a surprisingly high indistinguishability  $\mathcal{I} = 0.9999$  for the full hourglass structure for an on-axis QD. We attribute this high indistinguishability not to the mechanical effects but rather to the strong Purcell enhancement introduced by the cavity. Furthermore, we show that not only the efficiency but also the indistinguishability displays reasonable tolerance towards spatial misalignment of the QD. Thus, our work confirms that the performance of a low-dimensional structure, here the hourglass SPS, can indeed match or outperform more conventional SPS designs.

## ACKNOWLEDGEMENTS

The authors acknowledge support from the European Union's Horizon 2020 Research and Innovation Programme under the Marie Skłodowska-Curie Grant (Agreement No. 861097) and from the European Research Council (ERC-CoG "Unity", Grant No. 865230).

### Appendix A: Independent boson model

The emission spectrum  $S(\omega)$  is given by [24]

$$S(\omega) = \text{Re} \int_0^\infty dt P(t) e^{-\Gamma t/2} e^{-i\omega t}, \quad (\text{A1})$$

where  $P(t)$  denotes the coherence evolution of the system, which in turn, can be expressed as a function of the phonon propagator  $\Phi(t)$

$$\begin{aligned} P(t) &= e^{\Phi(t)} \\ &= \prod_m P_m(t) \\ &= \prod_m \exp[-\theta_m^2 \sin^2(\omega_m t/2) - \eta_m^2 (1 - e^{-i\omega_m t})]. \end{aligned} \quad (\text{A2})$$

Upon inspection of Eq. (A2), we can verify that the phonon propagator  $\Phi(t)$  corresponds to

$$\Phi(t) = \sum_m -\theta_m^2 \sin^2(\omega_m t/2) - \eta_m^2 (1 - e^{-i\omega_m t}). \quad (\text{A3})$$

Along with the phonon occupation number  $N_m$  given by Bose-Einstein statistics, we will employ the following definitions for the coupling parameters  $\theta_m^2$  and  $\eta_m^2$

$$\begin{cases} \theta_m^2 = 4\eta_m^2 N_m, & (\text{A4}) \\ \eta_m^2 = (g_m/\omega_m)^2, & (\text{A5}) \\ N_m = [\exp(\hbar\omega_m/k_B T) - 1]^{-1}. & (\text{A6}) \end{cases}$$

Here,  $k_B$  corresponds to the Boltzmann constant and  $T$  is the bath temperature. Also, we resort to the given trigonometric relations

$$\begin{cases} \sin^2(\omega_m t/2) = [1 - \cos(\omega_m t)]/2, & (\text{A7}) \\ \coth(\hbar\omega_m/2k_B T) = 1 + 2N_m. & (\text{A8}) \end{cases}$$

Now, making use of Eqs. (A4), (A5), and (A7) in Eq. (A3)

$$\Phi(t) = \sum_m \frac{g_m^2}{\omega_m^2} \left\{ -2N_m [1 - \cos(\omega_m t)] - 1 + e^{-i\omega_m t} \right\}. \quad (\text{A9})$$

Following, by isolating  $N_m$  from (A8) and plugging it into (A9), we are left with

$$\Phi(t) = \sum_m \frac{g_m^2}{\omega_m^2} \left\{ -[\coth(\hbar\omega_m/2k_B T) - 1][1 - \cos(\omega_m t)] - 1 + e^{-i\omega_m t} \right\}. \quad (\text{A10})$$

Lastly, developing the expression above, we can bring it to the following final form

$$\Phi(t) = \sum_m \frac{g_m^2}{\omega_m^2} \left\{ \coth\left(\frac{\hbar\omega_m}{2k_B T}\right) [\cos(\omega_m t) - 1] - i \sin(\omega_m t) \right\}, \quad (\text{A11})$$

which corresponds to the standard phonon propagator expression derived from the independent boson model [33].

- [1] R. P. Feynman, Simulating physics with computers, *Int J Theor Phys* **21**, 467 (1982).
- [2] 40 years of quantum computing, *Nat Rev Phys* **4**, 1 (2022).
- [3] A. Politi, J. C. F. Matthews, and J. L. O’Brien, Shor’s Quantum Factoring Algorithm on a Photonic Chip, *Science* **325**, 1221 (2009).
- [4] A. Crespi, R. Ramponi, R. Osellame, L. Sansoni, I. Bongioanni, F. Sciarrino, G. Vallone, and P. Mataloni, Integrated photonic quantum gates for polarization qubits, *Nat Commun* **2**, 566 (2011).
- [5] P. C. Humphreys, B. J. Metcalf, J. B. Spring, M. Moore, X.-M. Jin, M. Barbieri, W. S. Kolthammer, and I. A. Walmsley, Linear Optical Quantum Computing in a Single Spatial Mode, *Phys. Rev. Lett.* **111**, 150501 (2013).
- [6] H.-S. Zhong, H. Wang, Y.-H. Deng, M.-C. Chen, L.-C. Peng, Y.-H. Luo, J. Qin, D. Wu, X. Ding, Y. Hu, P. Hu, X.-Y. Yang, W.-J. Zhang, H. Li, Y. Li, X. Jiang, L. Gan, G. Yang, L. You, Z. Wang, L. Li, N.-L. Liu, C.-Y. Lu, and J.-W. Pan, Quantum computational advantage using photons, *Science* **370**, 1460 (2020).
- [7] N. Gregersen, D. P. S. McCutcheon, and J. Mørk, *Single-photon sources in Handbook of Optoelectronic Device Modeling and Simulation: Lasers, Modulators, Photodetectors, Solar Cells, and Numerical Methods*, 1st ed., edited by J. Piprek (CRC Press, Boca Raton, FL : CRC Press, Taylor & Francis Group, 2017) vol. 2, Chap. 46, pp. 585–607.
- [8] T. Heindel, J.-H. Kim, N. Gregersen, A. Rastelli, and S. Reitzenstein, Quantum dots for photonic quantum information technology, *Adv. Opt. Photon.* **15**, 613 (2023).
- [9] C. K. Hong, Z. Y. Ou, and L. Mandel, Measurement of subpicosecond time intervals between two photons by interference, *Phys. Rev. Lett.* **59**, 2044 (1987).
- [10] P. G. Kwiat, K. Mattle, H. Weinfurter, A. Zeilinger, A. V. Sergienko, and Y. Shih, New High-Intensity Source of Polarization-Entangled Photon Pairs, *Phys. Rev. Lett.* **75**, 4337 (1995).
- [11] P. Senellart, G. Solomon, and A. White, High-performance semiconductor quantum-dot single-photon sources, *Nature Nanotech* **12**, 1026 (2017).
- [12] H. Wang, Y.-M. He, T.-H. Chung, H. Hu, Y. Yu, S. Chen, X. Ding, M.-C. Chen, J. Qin, X. Yang, R.-Z. Liu, Z.-C. Duan, J.-P. Li, S. Gerhardt, K. Winkler, J. Jurkat, L.-J. Wang, N. Gregersen, Y.-H. Huo, Q. Dai, S. Yu, S. Höfling, C.-Y. Lu, and J.-W. Pan, Towards optimal single-photon sources from polarized microcavities, *Nat. Photonics* **13**, 770 (2019).
- [13] N. Tomm, A. Javadi, N. O. Antoniadis, D. Najer, M. C. Löbl, A. R. Korsch, R. Schott, S. R. Valentin, A. D. Wieck, A. Ludwig, and R. J. Warburton, A bright and fast source of coherent single photons, *Nat. Nanotechnol.* **16**, 399 (2021).
- [14] N. Maring, A. Fyrrillas, M. Pont, E. Ivanov, P. Stepanov, N. Margaria, W. Hease, A. Pishchagin, A. Lemaitre, I. Sagnes, T. H. Au, S. Boissier, E. Bertasi, A. Baert, M. Valdivia, M. Billard, O. Acar, A. Briessell, R. Mezher, S. C. Wein, A. Salavrakos, P. Sinnott, D. A. Fioretto, P.-E. Emeriau, N. Belabas, S. Mansfield, P. Senellart, J. Senellart, and N. Somaschi, A versatile single-photon-based quantum computing platform, *Nat. Photon.* **18**, 603 (2024).
- [15] J. Iles-Smith, D. P. S. McCutcheon, A. Nazir, and J. Mørk, Phonon scattering inhibits simultaneous near-unity efficiency and indistinguishability in semiconductor single-photon sources, *Nature Photon* **11**, 521 (2017).
- [16] B.-Y. Wang, E. V. Denning, U. M. Gür, C.-Y. Lu, and N. Gregersen, Micropillar single-photon source design for simultaneous near-unity efficiency and indistinguishability, *Phys. Rev. B* **102**, 125301 (2020).
- [17] A. D. Osterkryger, J. Claudon, J.-M. Gérard, and N. Gregersen, Photonic “hourglass” design for efficient quantum light emission, *Opt. Lett.* **44**, 2617 (2019).
- [18] B. Gaál, M. A. Jacobsen, L. Vannucci, J. Claudon, J.-M. Gérard, and N. Gregersen, Near-unity efficiency and photon indistinguishability for the “hourglass” single-photon source using suppression of the background emission, *Applied Physics Letters* **121**, 170501 (2022).
- [19] B.-Y. Wang, T. Häyrynen, L. Vannucci, M. A. Jacobsen, C.-Y. Lu, and N. Gregersen, Suppression of background emission for efficient single-photon generation in micropillar cavities, *Applied Physics Letters* **118**, 114003 (2021).
- [20] P. Tighineanu, C. Dreeßen, C. Flindt, P. Lodahl, and A. Sørensen, Phonon Decoherence of Quantum Dots in Photonic Structures: Broadening of the Zero-Phonon Line and the Role of Dimensionality, *Phys. Rev. Lett.* **120**, 257401 (2018).
- [21] N. Gregersen, D. P. S. McCutcheon, J. Mørk, J.-M. Gérard, and J. Claudon, A broadband tapered nanocavity for efficient nonclassical light emission, *Opt. Express* **24**, 20904 (2016).
- [22] S. Reitzenstein and A. Forchel, Quantum dot micropillars, *J. Phys. D: Appl. Phys.* **43**, 033001 (2010).
- [23] X. Ding, Y. He, Z.-C. Duan, N. Gregersen, M.-C. Chen, S. Unsleber, S. Maier, C. Schneider, M. Kamp, S. Höfling, C.-Y. Lu, and J.-W. Pan, On-Demand Single Photons with High Extraction Efficiency and Near-Unity Indistinguishability from a Resonantly Driven Quantum Dot in a Micropillar, *Phys. Rev. Lett.* **116**, 020401 (2016).
- [24] A. Artioli, S. Kotal, N. Gregersen, P. Verlot, J.-M. Gérard, and J. Claudon, Design of Quantum Dot-Nanowire Single-Photon Sources that are Immune to Thermomechanical Decoherence, *Phys. Rev. Lett.* **123**, 247403 (2019).
- [25] G. S. Pearson and D. A. Faux, Analytical solutions for strain in pyramidal quantum dots, *Journal of Applied Physics* **88**, 730 (2000).
- [26] P. Stepanov, M. Elzo-Aizarna, J. Bleuse, N. S. Malik, Y. Curé, E. Gautier, V. Favre-Nicolin, J.-M. Gérard, and J. Claudon, Large and Uniform Optical Emission Shifts in Quantum Dots Strained along Their Growth Axis, *Nano Lett.* **16**, 3215 (2016).
- [27] I. Vurgaftman, J. R. Meyer, and L. R. Ram-Mohan, Band parameters for III–V compound semiconductors and their alloys, *Journal of Applied Physics* **89**, 5815 (2001).
- [28] F. R. Braakman and M. Poggio, Force sensing with

- nanowire cantilevers, *Nanotechnology* **30**, 332001 (2019).
- [29] A. V. Lavrinenko, J. Lægsgaard, N. Gregersen, F. Schmidt, and T. Søndergaard, *Numerical Methods in Photonics*, 1st ed. (CRC Press, 2018).
- [30] U. M. Gür, S. Arslanagić, M. Mattes, and N. Gregersen, Open-geometry modal method based on transverse electric and transverse magnetic mode expansion for orthogonal curvilinear coordinates, *Phys. Rev. E* **103**, 033301 (2021).
- [31] M. Munsch, N. S. Malik, E. Dupuy, A. Delga, J. Bleuse, J.-M. Gérard, J. Claudon, N. Gregersen, and J. Mørk, Dielectric GaAs Antenna Ensuring an Efficient Broadband Coupling between an InAs Quantum Dot and a Gaussian Optical Beam, *Phys. Rev. Lett.* **110**, 177402 (2013).
- [32] M. Munsch, N. S. Malik, E. Dupuy, A. Delga, J. Bleuse, J.-M. Gérard, J. Claudon, N. Gregersen, and J. Mørk, Erratum: Dielectric GaAs Antenna Ensuring an Efficient Broadband Coupling between an InAs Quantum Dot and a Gaussian Optical Beam [Phys. Rev. Lett. **110**, 177402 (2013)], *Phys. Rev. Lett.* **111**, 239902 (2013).
- [33] A. Nazir and D. P. S. McCutcheon, Modelling exciton–phonon interactions in optically driven quantum dots, *J. Phys.: Condens. Matter* **28**, 103002 (2016).